Mon. Not. R. Astron. Soc. **000**, 1–13 (2014) Printed 27 February 2015 (MN LATEX style file v2.2)

Metallicity Measurements of Gamma-Ray Burst and Supernova Explosion Sites: Lessons from H II regions in M31

Yuu Niino[1⋆], Kentaro Nagamine[2,3] & Bing Zhang[3]
[1]*Division of Optical & Infrared Astronomy, National Astronomical Observatory of Japan, 2-21-1 Osawa, Mitaka, Tokyo 181-8588, Japan*
[2]*Department of Earth and Space Science, Graduate School of Science, Osaka University, 1-1 Machikaneyama-cho, Toyonaka, Osaka, 560-0043, Japan*
[3]*Department of Physics and Astronomy, University of Nevada, Las Vegas, 4505 S. Maryland Pkwy, Las Vegas, NV 89154-4002, U.S.A.*

arXiv:1408.7059v2 [astro-ph.HE] 26 Feb 2015

ABSTRACT
We examine how the small-scale ($<$ kpc) variation of metallicity within a galaxy, which is found in nearby galaxies, affect the observational estimates of metallicity in the explosion sites of transient events such as core-collapse supernovae (CC SNe) and gamma-ray bursts (GRBs). Assuming the same luminosity, metallicity, and spatial distributions of H II regions (hereafter HIIRs) as observed in M31, we compute the apparent metallicities that we would obtain when the spectrum of a target region is blended with those of surrounding HIIRs within the length scale of typical spatial resolution. When the spatial resolution of spectroscopy is $\lesssim 0.5$ kpc, which is typical for the existing studies of CC SN sites, we find that the apparent metallicities reflect the metallicities of target regions, but with significant systematic uncertainties in some cases. When the spatial resolution is $\gtrsim 1.0$ kpc, regardless of the target regions (which has a wide range of metallicity that spans ~ 0.6 dex for the M31 HIIRs), we always obtain the apparent metallicities similar to the average metallicity of the M31 HIIRs. Given that the apparent metallicities measured with $\gtrsim$kpc scale resolution do not necessarily reflect the immediate environment of the stellar explosions, the current observational estimates of high metallicities for some of the long GRB host galaxies do *not* rule out the hypothesis that the long GRBs are exclusively born in a low-metallicity environment.

Key words: gamma-ray burst: general – supernovae: general – galaxies: abundances – ISM: H II regions.

1 INTRODUCTION

The nature of the progenitors of stellar explosions is one of the most important questions in astronomy. It is generally agreed that type II, Ib, and Ic supernovae (core collapse supernovae, hereafter CC SNe) and most long-duration gamma-ray bursts (long GRBs) originate from core collapses of massive stars with $\gtrsim 8M_\odot$ at the end of their lives. Despite the above theoretical framework, the very physical reasons that define diverse supernova types and possible GRB associations with core collapse events are not clearly identified.

Some theoretical studies on the origin of GRBs using stellar evolution models suggest that a low metallicity may be a necessary condition for a GRB to occur ($Z <$ a few $\times\ 0.1Z_\odot$; e.g., Yoon & Langer 2005; Yoon et al. 2006; Woosley & Heger 2006). Observational studies have also shown that the metallicity distribution of the GRB host galaxies at redshifts $z \lesssim 1$ is significantly biased towards lower metallicities than that of general late-type galaxies at similar redshifts (Stanek et al. 2006; Graham & Fruchter 2013).

However, the metallicity of a host galaxy is not necessarily identical to that of the progenitor of a stellar explosion that occurs in it. There might be systematic differences between metallicities of the host galaxies and the progenitors. Niino (2011) discussed the metallicity distribution of galaxies that harbour low-metallicity star formation considering the observed properties of the local galaxies including the internal variation of metallicity within each galaxy, and showed that up to ~ 25 per cent of cosmic low-metallicity star formation with 12+log(O/H) < 8.2 takes place in high-metallicity galaxies with 12+log(O/H) > 8.8. To address this issue, some observational studies tried to spatially re-

⋆ E-mail: yuu.niino@nao.ac.jp

solve some GRB host galaxies and measure the metallicity of the local environment at the GRB sites (e.g., Modjaz et al. 2008). The systematic metallicity differences between the transient event sites and other parts of the host galaxies are actually observed in some cases (e.g., Levesque et al. 2011; Sanders et al. 2012b; Taddia et al. 2013). For long GRB host galaxies, the site metallicity tends to be lower than that in the other parts of galaxies. However, it is also claimed that the explosion sites of GRB 020819 (Levesque et al. 2010) and GRB 120422A (Schulze et al. 2014, but see also Levesque et al. 2012) have high metallicities.

The explosion site metallicities of CC SNe (e.g., Anderson et al. 2010; Modjaz et al. 2011; Galbany et al. 2014) are also systematically investigated. Among the major classes of CC SNe (II, Ib, and Ic), SNe Ib and Ic tend to occur in high-metallicity regions compared to SNe II (Anderson et al. 2010), although the difference of the site metallicities of type Ib and Ic SNe is still a matter of debate (Modjaz et al. 2011; Leloudas et al. 2011; Sanders et al. 2012b; Kuncarayakti et al. 2013). It is also suggested that metallicity plays an important role in the occurrence of some subclasses of CC SNe (Modjaz et al. 2011; Sanders et al. 2012a; Taddia et al. 2013; Lunnan et al. 2014).

It should be noted that we are not always able to resolve individual H II regions (HIIRs) that hosted GRBs and/or CC SNe, and hence the obtained spectra of the explosion sites may be blended with other neighboring HIIRs. In the context of supernova remnant (SNR) searches, Matonick & Fesen (1997) have shown that the observed number density of SNR is higher in nearer galaxies, because it becomes easier to resolve a confused region in a galaxy when it is nearby. We can expect that our capability to investigate the explosion site of a transient event would depend on the distance to the event (e.g., Sanders et al. 2012b, 2013; Taddia et al. 2013), as in the cases of SNR searches.

Recently, Sanders et al. (2012b) discussed how the metallicity measurements of Type Ibc SNe sites would be affected by the spatial resolution, assuming that an intrinsic metallicity difference of 0.2 dex is unrecognizable due to blending when the spatial resolution is worse than 2 kpc. Their results suggested that the blending does not significantly affect their SN sample whose typical redshift is < 0.1. However, it is not known what spatial resolution is really necessary to probe the immediate environment of a transient, which would be closely connected to the nature of the progenitor star. Especially for GRBs that typically occur at redshifts $\gtrsim$ a few $\times$ 0.1, the typical spatial resolution of ground-based observations ($\sim$ 1 arcsec) corresponds to a few kpc, which is often limited by the seeing of atmosphere (not instrument). Therefore it is likely that there is some metallicity variation below the resolution limit.

The internal metallicity structure of galaxies have been studied for decades. It is broadly agreed that the metallicity decreases as the galactocentric radius increases in many galaxies (so-called metallicity gradient, e.g., Shields & Searle 1978; Zaritsky et al. 1994), while slope of the gradient may vary within a galaxy (e.g., Luck et al. 2003; Bresolin et al. 2009; Balser et al. 2011; Esteban et al. 2013), and a significant scatter of metallicity around the gradient may also exist (e.g., Afflerbach et al. 1997; Rosolowsky & Simon 2008). Some recent studies intensely performed integral field spectroscopic (IFS) observations of nearby late type galaxies (e.g., Rosales-Ortega et al. 2010; Mármol-Queraltó et al. 2011; Sánchez et al. 2012; Fogarty et al. 2012; Blanc et al. 2013; Richards et al. 2014; Belfiore et al. 2014), and dramatically increased the sample size of HIIRs with measured metallicities. Furthermore, Sanders et al. (2012c, hereafter S12) obtained the spectra of > 200 HIIRs in M31 (the Andromeda galaxy), and found that $\sim 1/3$ of the HIIR pairs with separations less than 500 pc show significant (i.e., larger than the error) metallicity variation.

In this paper, we examine how the metallicity estimates from spectroscopic observations are affected by limited resolution. We do this by performing mock blended observations with limited resolution, assuming the same observed distributions of emission-line luminosities and line ratios as the M31 HIIRs.

The remaining part of the paper is organized as follows. In §2, we describe the spectroscopic and photometric data sets that we use in this study. In §3, we discuss the variation of metallicity among the M31 HIIRs, especially on small scales ($\lesssim$ kpc). In §4, we discuss the line luminosities of HIIRs. In §5, we demonstrate the degree of bias in the measured metallicity caused by the small-scale variation in metallicity. In §7, we discuss the implications for the current observations of the explosion sites of transient events. We summarise our conclusions in §8.

2 DATA SETS

We use the observed properties of the HIIRs in M31 to investigate how the spatial resolution limit affects the metallicity estimates of explosion sites. M31 is an irreplaceable laboratory to study the small-scale variation of metallicity in interstellar medium (ISM) of a late type galaxy. In M31, the structures of HIIRs are resolved down to < 10 pc (e.g., Massey et al. 2007; Azimlu et al. 2011), and spectroscopic information is available for more than 200 HIIRs (S12). The HIIRs in the Magellanic clouds have also been studied for decades, however, the number of spectroscopic sample is small for a statistical study ($\sim$ 20; e.g., Dufour & Harlow 1977; Pagel et al. 1978; Vermeij et al. 2002). Although the observed sample size of HIIRs in other local late-type galaxies was significantly increased by the recent IFS surveys, their spatial resolution was $\gtrsim 100$ pc except for a few cases (Sánchez et al. 2012, 2014), and many HIIRs that have a spatial extent of $\lesssim$ several 10 pc are not resolved.

Azimlu et al. (2011, hereafter A11) constructed a photometric sample of HIIRs based on broad- and narrow-band images taken by the Local Group Galaxies Survey (LGGS, Massey et al. 2006), covering the whole disk of M31. The sample contains 3961 HIIRs with Hα luminosities $L_{\mathrm{H}\alpha} \gtrsim 10^{34.5}$ erg s^{-1}, excluding known and potential planetary nebulae (PNe). The largest spectroscopic sample of HIIRs in M31 was constructed by S12, who obtained the spectra of 253 HIIRs and 407 PNe, selected from the LGGS images and some samples of emission line objects in the literature.

In this study, we use the photometric and spectroscopic sample of the M31 HIIRs provided by A11 and S12 to examine how the spatial resolution affects the observed properties of transient event sites. Following S12, we obtain the HIIR positions in a deprojected coordinate on the disk of M31

assuming the following quantities: the inclination angle of 12°.5 (Simien et al. 1978); the distance to M31 of 770 kpc (Freedman & Madore 1990); the position of M31 center (α, δ) and the angle of disk major axis relative to north celestial pole (ϕ) as

$$\alpha = 00^\circ 42' 44''.52 \text{ (J2000)}, \quad (1)$$
$$\delta = +41^\circ 16' 08''.69 \text{ (J2000)}, \quad (2)$$
$$\phi = 37^\circ 42' 54'' \quad (3)$$

(Baade & Arp 1964).

3 METALLICITIES OF THE H II REGIONS

3.1 Metallicity diagnostics

S12 obtained the fluxes of following emission lines: [O II] λ3727, [O III] $\lambda\lambda$4363,4959,5007, Hβ, [N II] $\lambda\lambda$6548,6584, Hα, and [S II] $\lambda\lambda$6717,6731. Not all of these lines are detected for all HIIRs in the S12 sample. It should be noted that S12 obtained the line fluxes with 1.5 arcsec fibers. The fiber loss corrections are not available in S12, thus the fluxes are different from the total fluxes. Therefore we only use the ratio between different lines in S12 sample, but not the absolute flux values.

Various metallicity calibration methods are proposed to measure the metallicity of ionized gas in HIIRs. However, the results of different calibration methods are not always consistent with each other (e.g., Kennicutt et al. 2003; Kewley & Ellison 2008; López-Sánchez et al. 2012). In order to maximize our sample size with metallicity estimates, we mainly use the N2 index = $\log_{10}$[N II]/Hα as a metallicity indicator (hereafter [N II] means [N II] λ6584 unless otherwise specified). Among the 253 HIIRs in the S12 sample, Hα and [N II] lines are detected for 222 HIIRs with flux errors < 20 per cent, while [O III] λ5007, which is also widely used to measure the HIIR metallicity, is detected only for 58 HIIRs with flux errors < 20 per cent. We also discuss the analysis with other metallicity indicators in §6. The metallicity indices are corrected for dust extinction using the extinction curve by Cardelli et al. (1989, $R_V = 3.1$) and A_V of each HIIR, which were derived by S12 assuming an intrinsic value of Hα/Hβ = 2.85 and Cardelli's extinction curve.

We assume a relation between the N2 index and 12+log(O/H) empirically calibrated by Marino et al. (2013) using an observed sample of HIIRs in local galaxies with metallicity measurements by the 'direct' method (e.g., Garnett 1992). It should be noted that the N2 index and many other metallicity indicators are also affected by the physical conditions of gas other than metallicity, such as the ionization state (e.g., McGaugh 1991; Pilyugin 2000; Kewley & Dopita 2002; López-Sánchez et al. 2011). Marino et al. (2013) calibrated the N2 index with the HIIRs in local galaxies which would have physical conditions close to those of the M31 HIIRs discussed here, compared to the case of the calibrations based on galaxy scale observations (e.g., Nagao et al. 2006; Maiolino et al. 2008).

It is known that the N2 index saturates when metallicity is high, and hence cannot be used to measure the high metallicity in some HIIRs. In the calibration by Marino et al. (2013), the N2 index saturates when 12+log(O/H) $\gtrsim$ 8.7 (N2 > -0.2), and we cannot determine the metallicity when the N2 index is higher than this value. S12 excluded the HIIRs with undetermined metallicities from their sample. Instead, we include all HIIRs with Hα and [N II] detections in our sample, assuming that the HIIRs with N2 > -0.2 have higher metallicities than those with lower N2 index [i.e., 12+log(O/H)$_{\rm N2}$ $\gtrsim$ 8.7].

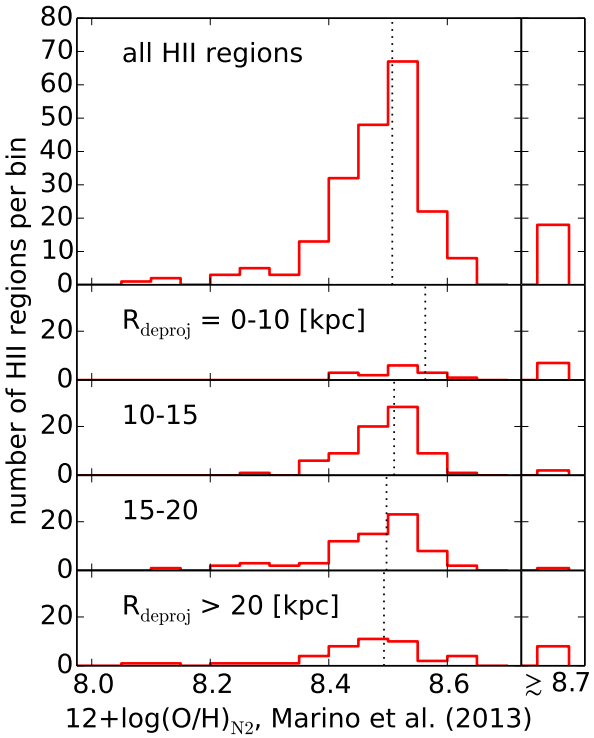

Figure 1. Metallicity distribution of the M31 HIIRs in the S12 sample, measured with the N2 index calibrated by Marino et al. (2013). The top panel shows the distribution of all M31 HIIRs, and the other panels show the distributions at deprojected galactocentric radii $R_{\rm deproj}$ = 0–10, 10–15, 15–20 and > 20 kpc. The number of HIIRs with N2 > -0.2 (i.e., 12+log(O/H)$_{\rm N2}$ $\gtrsim$ 8.7) is shown separately in the right-hand-side of each panel. The vertical dotted lines represent the median of each distributions including the HIIRs with N2 > -0.2.

3.2 Metallicity variation in M31

We show the metallicity distribution of all M31 HIIRs in the top panel of Figure 1. In the bottom 4 panels of Figure 1, the sample is divided into 4 subsamples according to the deprojected galactocentric radius ($R_{\rm deproj}$). The HIIR metallicities at larger $R_{\rm deproj}$ are systematically lower. The large intrinsic scatter of metallicity discussed in S12 is clearly seen in each $R_{\rm deproj}$ bin. Marino et al. (2013) showed that the intrinsic error of their N2 index calibration $\pm$0.16 dex (or $\pm$0.09 dex depending on the calibration data sets). Although the scatter may be partly due to the intrinsic error in the metallicity calibration methods, S12 showed that the HIIR-metallicity distributions in M31 have similarly large scatters when they are measured by various calibration methods, some of which have the intrinsic errors $\lesssim$ 0.1 dex (Kewley & Ellison 2008), We also discuss other metallicity calibration methods in §6.

S12 pointed out that 33 per cent of the close HIIR pairs

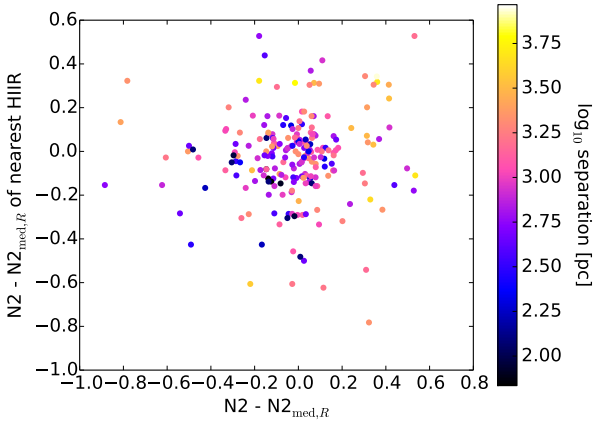

Figure 2. Comparison of the N2 index deviation of each HIIR from the median N2 in each radial bin (N2−N2$_{\mathrm{med},R}$) and that of the nearest one in the S12 sample. Separations of the HIIR pairs on the disk of M31 are colour-coded from dark blue (close, ~ 100 pc) to bright yellow (distant, ~ 8 kpc).

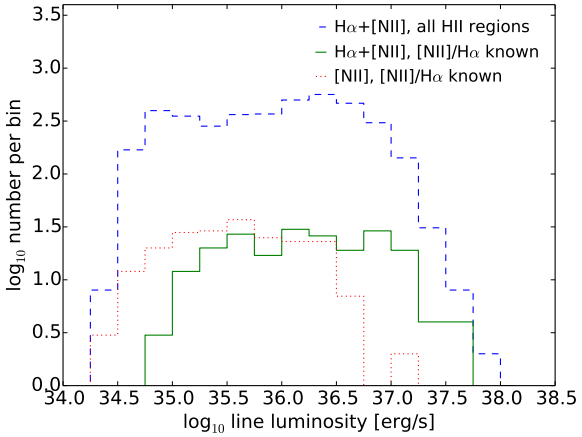

Figure 3. Hα and [N II] emission line luminosity distributions of M31 HIIRs without dust correction. The dashed line shows the Hα+[N II] flux distribution of all A11 HIIRs including those without known N2 index. For those with known N2 index in the S11 sample, the distributions of Hα+[N II] flux (solid) and [N II] flux (dotted) are plotted. The line luminosities of S11 HIIRs are obtained by matching them to the A11 sample as described in the main text (§4).

(with deprojected separations < 0.5 kpc) show metallicity variation of more than 0.3 dex. To further investigate the metallicity variation on small scales, we compare the N2 index of each HIIR and the nearest one for which N2 index is available. We divide the S12 sample into four different bins of R_{deproj} (0–10, 10–15, 15–20, and > 20 kpc, as shown in Figure 1), and consider the deviation of N2 index of each HIIR from the median N2 in each radial bin (N2−N2$_{\mathrm{med},R}$) to investigate the metallicity scatter separately from the metallicity gradient. In Figure 2, we plot N2−N2$_{\mathrm{med},R}$ of each HIIR and N2−N2$_{\mathrm{med},R}$ of the nearest one to the HIIR. We do not find any significant correlation between N2−N2$_{\mathrm{med},R}$ of the neighboring HIIR pairs including the cases with the deprojected separation of a few 100 pc. This suggests that the ISM in M31 is not mixed efficiently, and that the ISM metallicity varies even on small scales of a few 100 pc.

4 LINE LUMINOSITIES OF THE H II REGIONS

The emission-line luminosity distribution of HIIRs is also an important issue when we discuss the blending of HIIRs in spectroscopy with limited spatial resolution. When we spectroscopically observe multiple HIIRs blended within spatial resolution, the one with stronger line emissions affects the resulting spectrum more, although the less luminous HIIRs in an emission line might be bright in other lines depending on their physical conditions such as metallicity and/or ionization state.

To obtain the emission line luminosities of S12 HIIRs, we match the S12 sample to the photometric sample of A11, because the fiber-corrected total luminosity is not available for the S12 sample. We match each S12 HIIR to an A11 HIIR individually when the separation between the fiber position of the S12 HIIR and the flux peak location of the A11 HIIR is smaller than the HIIR radius determined by A11, and the S12 HIIR of concern is the nearest HIIR in the S12 sample to the A11 HIIR. It should be noted that, when the Hα emission is extended with multiple intensity peaks, the HIIR detection method used in A11 separates the object into multiple HIIRs. In such a case, it is possible that multiple A11 HIIRs match with a single S12 HIIR, in which case we assign the sum of the A11 HIIR luminosities to the corresponding S12 HIIR. Among the 222 HIIRs with known N2 index in the S12 sample, 197 have one or more counterparts in the A11 sample.

To find the line emitting regions in M31, A11 used the Hα narrow-band images with continuum subtraction based on the R-band images. The narrow-band contains Hα and [N II] lines, and A11 corrected the [N II] line contamination to obtain the Hα flux assuming a global line ratio of [N II]/Hα = 0.35. We undo this [N II] correction and recalculate the Hα and [N II] fluxes based on the N2 index of each HIIR obtained by S12.

Figure 3 compares the Hα+[N II] luminosity distribution of the S12 HIIRs with Hα and [N II] detections (solid line) to that of all A11 HIIRs (dashed line). Although the spectroscopic observations are performed only for a small fraction of the detected HIIRs, the sample with Hα and [N II] detections covers a wide range of line luminosity, $35.0 < \log_{10} L_{\mathrm{H}\alpha+[\mathrm{N\,II}]}[\mathrm{erg\ s^{-1}}] < 37.5$, while [N II] is hardly observed for HIIRs with $\log_{10} L_{\mathrm{H}\alpha+[\mathrm{N\,II}]}[\mathrm{erg\ s^{-1}}] < 35.0$. We also plot the [N II] luminosity distribution for the sample with Hα and [N II] detections (dotted line). The faint end of the [N II] luminosity distribution suggests that the effective limiting luminosity for a line detection in the S12 spectroscopy was $\log_{10} L[\mathrm{erg\ s^{-1}}] \sim 34.5$, which is close to the limiting luminosity of the A11 sample. The [N II] luminosity distribution is ~ 0.5 dex fainter than the Hα+[N II] luminosity distribution of the same sample, reflecting the typical N2 index ~ -0.5 in M31.

Now let us consider a case where one tries to obtain the emission line ratio of a specific HIIR of interest (such as an explosion site of a GRB/CC SN) without sufficient spatial resolution to separate the HIIR from the surrounding ones.

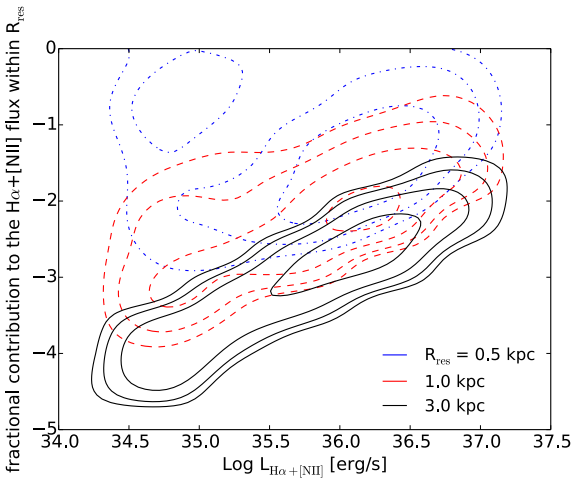

Figure 4. Distributions of the A11 HIIRs on the $L_{\mathrm{H}\alpha+[\mathrm{N\,II}]}$ vs. fractional contribution plane with $R_{\mathrm{res}} = 0.5$, 1.0, and 3.0 kpc (dot-dashed, dashed, and solid, respectively). The contours indicate the surface number density of 100, 200, 400, and 800 dex^{-2}.

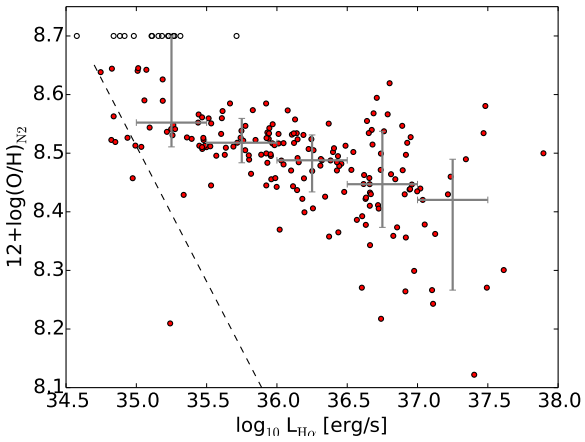

Figure 5. Hα luminosities and metallicities of the HIIRs with known N2 index. The open circles at the top represent the HIIRs with N2 > -0.2, for which the metallicities are not determined well. The dashed line represents the constant [N II] luminosity of $10^{34.5}$ erg s^{-1}. The error bars indicate the median and 68 percentile scatter in the five bins of $L_{\mathrm{H}\alpha}$ with the log-scale width of 0.5 dex in the range of $\log_{10} L_{\mathrm{H}\alpha}$ [erg s^{-1}] = 35.0–37.5.

If the HIIR of interest is bright enough to dominate the total flux within the spatial resolution, we obtain the metallicity of the HIIR regardless of the metallicity distribution of surrounding HIIRs. When we observe the explosion site of a long GRB and/or a SN Ic, the HIIR that hosted the transient is expected to be brighter than the other HIIRs, because the progenitors of these explosions are likely very young (Fruchter et al. 2006; Kelly et al. 2008; Leloudas et al. 2010).

Using the photometric sample of 3961 HIIRs by A11, we investigate the fractional contribution of each HIIR to the total Hα luminosity within the resolution scale radius R_{res} in the deprojected disk coordinate. Here, the fractional contribution means the fraction of $L_{\mathrm{H}\alpha+[\mathrm{N\,II}]}$ to the total Hα+[N II] luminosity of all HIIR within R_{res}. Figure 4 shows the fractional contributions of the A11 HIIRs versus $L_{\mathrm{H}\alpha}$ for different R_{res}. For $R_{\mathrm{res}} \gtrsim 1.0$ kpc, even the most brightest HIIR have a typical fractional contribution of $\lesssim 10$ per cent, suggesting a significant blending effect on emission-line measurements.

Figure 5 plots $L_{\mathrm{H}\alpha}$ versus metallicity of HIIRs with known N2 indices. It is clear that the brighter HIIRs tend to have lower metallicities. One possible cause of this trend is the non-detection of [N II] lines for the faint HIIRs. The N2 index positively correlates with metallicity, therefore it would be difficult to detect the [N II] line of a faint, metal-poor HIIR. The dashed line in Figure 5 shows the relation for a fixed [N II] luminosity of $10^{34.5}$ erg s^{-1}. At the lowest $L_{\mathrm{H}\alpha}$, high-metallicity HIIRs naively follow this relation, but the low-metallicity HIIRs typically have much larger $L_{\mathrm{H}\alpha}$. Hence it might be difficult to explain the $L_{\mathrm{H}\alpha}$–metallicity relation only by a single limiting flux. We note that the line detection limit may not be uniform over the entire M31 disk, as it is affected by the variation of the background radiation from diffuse interstellar gas (A11), and there might be PN contaminations in faint, high-metallicity HIIRs (S12).

5 METALLICITY MEASUREMENTS WITH LIMITED SPATIAL RESOLUTION

The small-scale metallicity variation and the luminosity distribution of HIIRs discussed in previous sections suggest that the observed spectroscopic properties of GRB/CC SN sites will be largely affected by the blending with nearby HIIRs. In this section, we discuss what spatial resolution would be necessary to obtain a reliable metallicity for a GRB/CC SN site, and how the observed metallicities differ from the intrinsic ones under the observations with insufficient spatial resolution. In the following, we define the "apparent metallicity" of an HIIR for a resolution scale radius of R_{res} as a metallicity inferred from the ratio of total Hα and [N II] line fluxes of all HIIRs inside R_{res}.

As mentioned in §2, the sampling rate of spectroscopic sample is low, and the N2 index is not available for most A11 HIIRs. For demonstration purposes, we assume that the HIIRs with unknown N2 index follows the same N2 index distribution as found in the S12 sample. We divide the S12 sample into four different bins of R_{deproj} (0–10, 10–15, 15–20, and > 20 kpc, Figure 1) and examine the effect of metallicity gradient.

Practically, the apparent metallicities are calculated as follows. For each HIIR with Hα and [N II] detections in S12, we collect all HIIRs from the A11 sample which reside within a given radius of R_{res} (deprojected), and sum up the Hα and [N II] fluxes. For an A11 HIIR that has a matched S12 HIIR with a known N2 index, the Hα and [N II] fluxes are calculated assuming the index value (see §4 for the sample matching method). When the N2 index is not available for an A11 HIIR, we randomly select an S12 HIIR in the same R_{deproj} bin with Hα and [N II] detections. Then we calculate the Hα and [N II] fluxes of the A11 HIIR assuming the same N2 index to that of the selected S12 HIIR. We repeat this random realisation of apparent metallicities 100 times for

each of 197 HIIRs with known N2 index and photometric counterparts.

We show the intrinsic versus apparent metallicities of HIIRs in Figure 6 for $R_{\rm res}$ = 0.1, 0.3, 0.5, 1.0, 2.0, and 3.0 kpc. When $R_{\rm res} \geqslant 1$ kpc, the HIIRs with lower (higher) intrinsic metallicities than $12+\log({\rm O/H})_{\rm N2} = 8.5$ have systematically higher (lower) apparent metallicities than the intrinsic values. This is because most of the contaminating HIIRs have N2 indices that correspond to 12+log(O/H) = 8.4–8.6 (Figure 1). In this case, it is difficult to distinguish low-metallicity HIIRs from high-metallicity ones, because all HIIRs with intrinsic $12+\log({\rm O/H})_{\rm N2}$ = 8.2–8.7 have similar apparent metallicities within the scatter. With $R_{\rm res} \leqslant 0.5$ kpc, the apparent metallicity correlates well with the intrinsic value, although some systematic differences exist for $R_{\rm res} = 0.5$ kpc.

As discussed in §4, the metallicities of low-luminosity HIIRs may be biased towards high metallicities (Figure 5). To investigate how the possible bias affects our results, we also compute the apparent metallicities considering the N2 index distribution of only bright HIIRs with $\log_{10} L_{\rm H\alpha}[{\rm erg\ s^{-1}}] > 36.5$ in the S12 sample when we randomly determine the N2 index of an A11 HIIR with unknown N2 index. We did not find significant differences between the results obtained with the N2 index distribution of bright HIIRs and those with all HIIRs, except that the apparent metallicities computed with the bright HIIRs are slightly lower (by < 0.1 dex) than those in Figure 6 for $R_{\rm res} \geqslant 1.0$ kpc.

In Figure 7, we quantify the deviation between the intrinsic and apparent metallicities in a different way from Figure 6, by presenting the distributions of ΔN2 = $\mathrm{N2_{apparent}} - \mathrm{N2_{intrinsic}}$ for low-, intermediate-, and high-metallicity HIIRs (i.e., intrinsic N2 index of < -0.7, $-0.7 \leqslant$ N2 < -0.4, and $-0.4 \leqslant$ N2, respectively) with $R_{\rm res}$ = 0.1, 0.5, and 2.0 kpc. For $R_{\rm res}$ = 0.1 kpc, the majority of HIIRs have $|\Delta{\rm N2}| < 0.1$ for all ranges of intrinsic metallicity. For $R_{\rm res}$ = 0.5 kpc, the ΔN2 distribution still peaks at around zero, although there is a systematic difference between the $\mathrm{N2_{intrinsic}}$ and $\mathrm{N2_{apparent}}$ [i.e., $\Delta{\rm N2} > 0$ for low-metallicity HIIRs and < 0 for high-metallicity ones, which is consistent with what we see in Figure 6]. For $R_{\rm res}$ = 2.0 kpc, there is no peak at $\Delta \log_{10}({\rm O/H}) = 0$ either for low- or high-metallicity HIIRs, meaning that the intrinsic and apparent metallicities do not agree with each other.

We note that the metallicity variation in each HIIR is not considered in our analysis. Observations of some giant HIIRs in the Milky Way and the Magellanic clouds have shown that the metallicity variation within each HIIR is typically within $\pm$0.1 dex in most parts of the HIIRs (e.g., Lebouteiller et al. 2008; Mesa-Delgado et al. 2008; Mesa-Delgado & Esteban 2010). Thus we consider that the metallicity variation within each HIIR is smaller compared to that between different HIIRs. As mentioned in §3.1, the N2 index and many other metallicity indicators are also affected by the physical conditions of gas other than metallicity. Hence it is unclear to what extent the observed variation of line ratios in M31 originates from the metallicity variation. However, we can at least conclude that there is a difficulty in measuring the intrinsic line ratio of a transient event site with $R_{\rm res} \geqslant 1$ kpc.

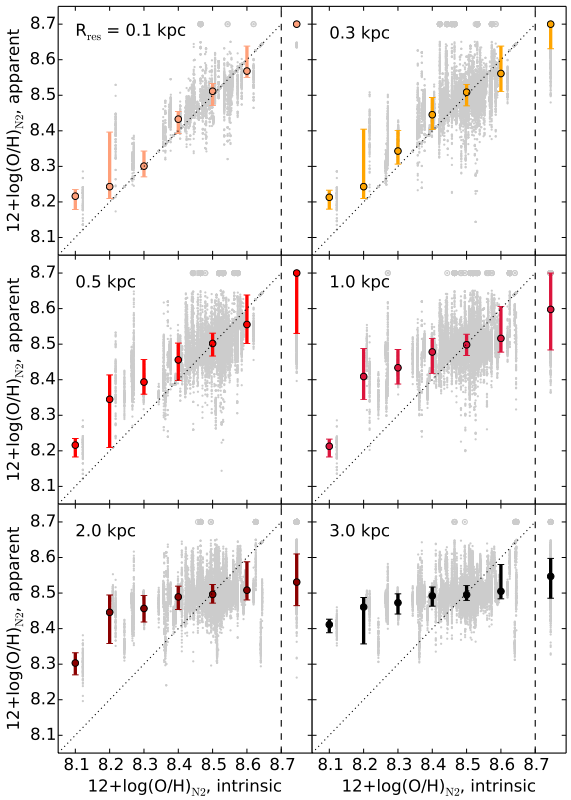

Figure 6. Intrinsic versus apparent metallicities of HIIRs with known N2 index for various $R_{\rm res}$. The grey dots represent each data points (197 HIIRs × 100 random realisations of apparent metallicity in each panel). The grey circles at the top of each panel represent the data with apparent N2 > -0.2. The data points with intrinsic N2 > -0.2 are plotted separately in the right-hand-side of each panel. The circles and the error bars indicate median and 68 percentile scatter of the data points in intrinsic metallicity bins (bin width of 0.2 dex). The data points with apparent N2 > -0.2 are included in the median and scatter calculation. The diagonal dotted line indicates the equality between the apparent and intrinsic metallicities.

6 OTHER METALLICITY INDEXES

In this section, we discuss how the blending effect appears when we measure the HIIR metallicities with indicators other than N2 index. Here we consider, O3N2 index = $\log_{10}[([{\rm O\,III}]\ \lambda5007/{\rm H}\beta)\times({\rm H}\alpha/[{\rm N\,II}])]$, N2O2 index = $\log_{10}([{\rm N\,II}]/[{\rm O\,II}]\ \lambda3727)$, and R_{23} index = $([{\rm O\,II}]\ \lambda3727+[{\rm O\,III}]\ \lambda\lambda4959, 5007)/{\rm H}\beta$, which are available with flux errors < 20 per cent for 58, 98, and 60 HIIRs, respectively. For the O3N2 indices, we use the metallicity calibration by Marino et al. (2013) based on the same HIIR sample as the N2 calibration. For O2N2 and R_{23} indices, we use the theoretical calibration by Kewley & Dopita (2002, KD02) and Kobulnicky & Kewley (2004, KK04), respectively.

It is known that the R_{23} index provides two solutions of possible metallicities, one in the upper branch [$12+\log({\rm O/H})_{R23} > 8.4$], and the other in the lower branch [$12+\log({\rm O/H})_{R23} < 8.4$]. KK04 showed that the HIIRs with

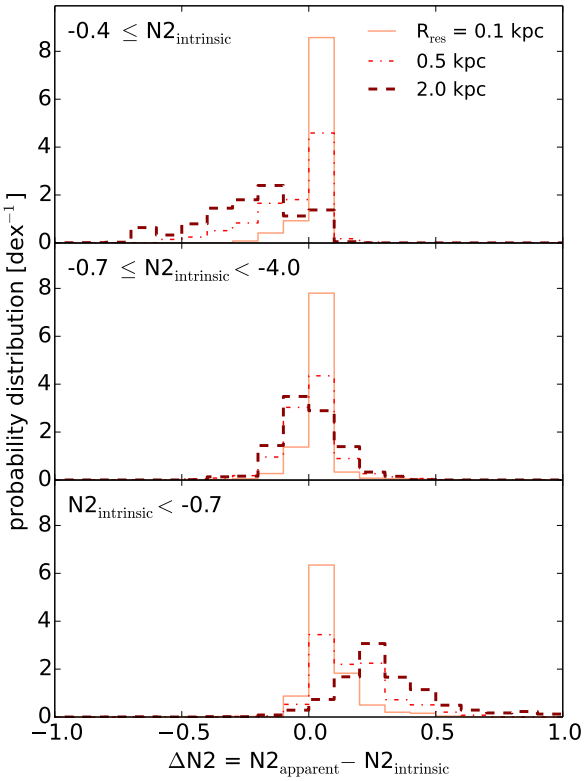

Figure 7. Probability distribution of difference between the intrinsic and apparent N2 index: ΔN2 = N2$_{\rm apparent}$ − N2$_{\rm intrinsic}$. We divide the sample into the following three different ranges: N2 < -0.7 (bottom), $-0.7 \leqslant$ N2 < -0.4 (middle), and $-0.4 \leqslant$ N2 (top panel).

12+log(O/H)$_{R23} < 8.4$ hardly have N2 > -1.0, while more than 95 per cent of the S12 HIIR with N2 index have N2 > -1.0 [12+log(O/H)$_{\rm N2} > 8.28$ in the calibration by Marino et al. (2013), see Figure 1]. Therefore, we assume the upper branch solutions for the M31 HIIRs, although some HIIRs with N2 < -1.0 may have lower-branch metallicities.

Similarly to the N2 index, other indices (O3N2, N2O2, and R_{23}) are calibrated to metallicity only in some limited ranges. In Marino et al. (2013), the O3N2 index is calibrated within $-1.1 <$ O3N2 < 1.7 which corresponds to $8.17 <$ 12+log(O/H) $_{\rm O3N2} < 8.77$, and the metallicity cannot be measured correctly with the O3N2 index out of this range. A few of the S12 HIIR have O3N2 > 1.7, and we assume that these HIIRs have 12+log(O/H)$_{\rm O3N2} \lesssim 8.0$ (O3N2 index anti-correlates with metallicity). The N2O2 index is sensitive to metallicity when N2O2 > -0.97 [or 12+log(O/H)$_{\rm N2O2} >$ 8.6, KD02], and we assume that the HIIRs with N2O2 $\leqslant -0.97$ have 12+log(O/H)$_{\rm N2O2} \lesssim 8.5$. The R_{23} index is calibrated at $\log_{10}R_{23} \lesssim 1.0$ depending on an additional parameter O_{32} = ([O III] $\lambda\lambda$4959, 5007/[O II] λ3727). All S12 HIIRs with R_{23} index have the values of R_{23} and O_{32} in the calibrated ranges.

We show the metallicity distributions of M31 HIIRs measured with O3N2, N2O2, and R_{23} indices in Figure 8. As previously reported, the theoretically calibrated methods give systematically higher metallicities than the empirical calibrations based on the 'direct' method (Kewley & Ellison 2008; López-Sánchez & Esteban 2010). The median 12+log(O/H) measured with N2, O3N2, N2O2, and R_{23} indices are 8.51, 8.38, 8.85, and 8.81, respectively. All metallicity indices discussed here commonly have wide distributions of 12+log(O/H) spanning ~ 0.6 dex with different sample sizes. The calibration of O3N2 index by Marino et al. (2013) has intrinsic errors of $\pm$0.08–0.18 dex depending on the HIIR sample used for the calibration, while Kewley & Ellison (2008) suggested that the calibrations by KD02 and KK04 have intrinsic error of 0.06 dex. The metallicity gradient is more significant with O3N2, N2O2, and R_{23} indices than with N2 index, while the large scatter in each $R_{\rm deproj}$ is commonly seen. We note that the dependence of metallicity gradient on metallicity calibration method is also reported by S12. The N2O2 index possibly shows a multi-peak metallicity distribution at $R_{\rm deproj} > 20$ kpc which is not seen with other metallicity indices.

Here we investigate the small-scale scatter of different metallicity indices similarly to §3.2. The upper left, upper right, and lower left panels of Figure 9 show the scatter of O3N2, N2O2, and R_{23} indices, respectively. We discuss the scatter of the indices rather than the metallicity in order to include the HIIRs which have index values outside the calibrated range. While all three indices show large scatters similarly to the N2 index (Figure 2), the N2O2 index also shows some correlations between the metallicities of neighboring HIIR pairs. The N2O2 index is not largely affected by the gas ionization state, however it suffers largely from the uncertainty of extinction correction (KD02). The calibration of R_{23} index by KK04 also reduces the effect of ionization state using the additional parameter O_{32}, therefore the R_{23} index and the metallicity do not correspond one-to-one. In the lower right panel of Figure 9, we show the scatter of log(O/H) measured by the R_{23} index (including O_{32}). With the O_{32} parameter included, log(O/H)$_{R23}$ of the neighboring HIIR pairs show a large scatter as well as $\log_{10}R_{23}$ itself. This suggests that the variation of ionization state is not the dominant source of the scatter seen in Figure 2 and 9.

In Figure 10, we plot $L_{\rm H\alpha}$ versus metallicity of HIIRs measured with O3N2, N2O2, and R_{23} indices. The O3N2 and R_{23} indices (the top and bottom panels, respectively) are rarely available for faint HIIRs with $\log_{10}L_{\rm H\alpha}$ [erg s^{-1}] < 36.0. However, a small number of faint HIIRs with O3N2 index have systematically higher 12+log(O/H)$_{\rm O3N2}$ than the HIIRs with larger $L_{\rm H\alpha}$, which is consistent with the trend found with the N2 index. On the other hand, such a trend is not seen with R_{23}. With the N2O2 index, the metallicity is constant over a wide range of Hα luminosity, $35.5 <$ $\log_{10}L_{\rm H\alpha}$ [erg s^{-1}] < 37.5 (or possibly higher metallicity with larger $L_{\rm H\alpha}$), although the faintest HIIRs with $\log_{10}L_{\rm H\alpha}$ [erg s^{-1}] ~ 35 have systematically higher metallicities than those with larger $L_{\rm H\alpha}$. The dependence of $L_{\rm H\alpha}$–metallicity relation on the metallicity indicator suggests that the relation is produced by some artificial effect, although it is difficult to draw robust conclusions.

In Figure 11, we show the relation between the intrinsic and apparent metallicities using the O3N2, N2O2, and R_{23} indices with $R_{\rm res} = 0.1$, 0.5, and 2.0 kpc The apparent metallicities are computed following the same method as for the N2 index (§5). Although the absolute metallicity scale is different for different metallicity indices, the relations be-

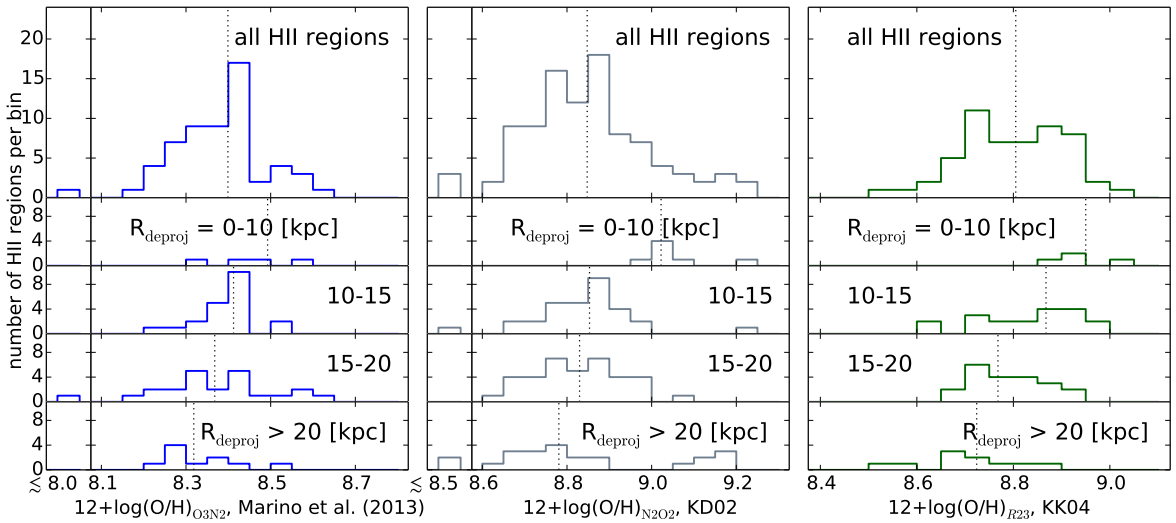

Figure 8. Same as Figure 1, but for the metallicities measured with O3N2 (left), N2O2 (middle), and R_{23} (right panel) indices using calibrations by Marino et al. (2013), KD02, and KK04, respectively.

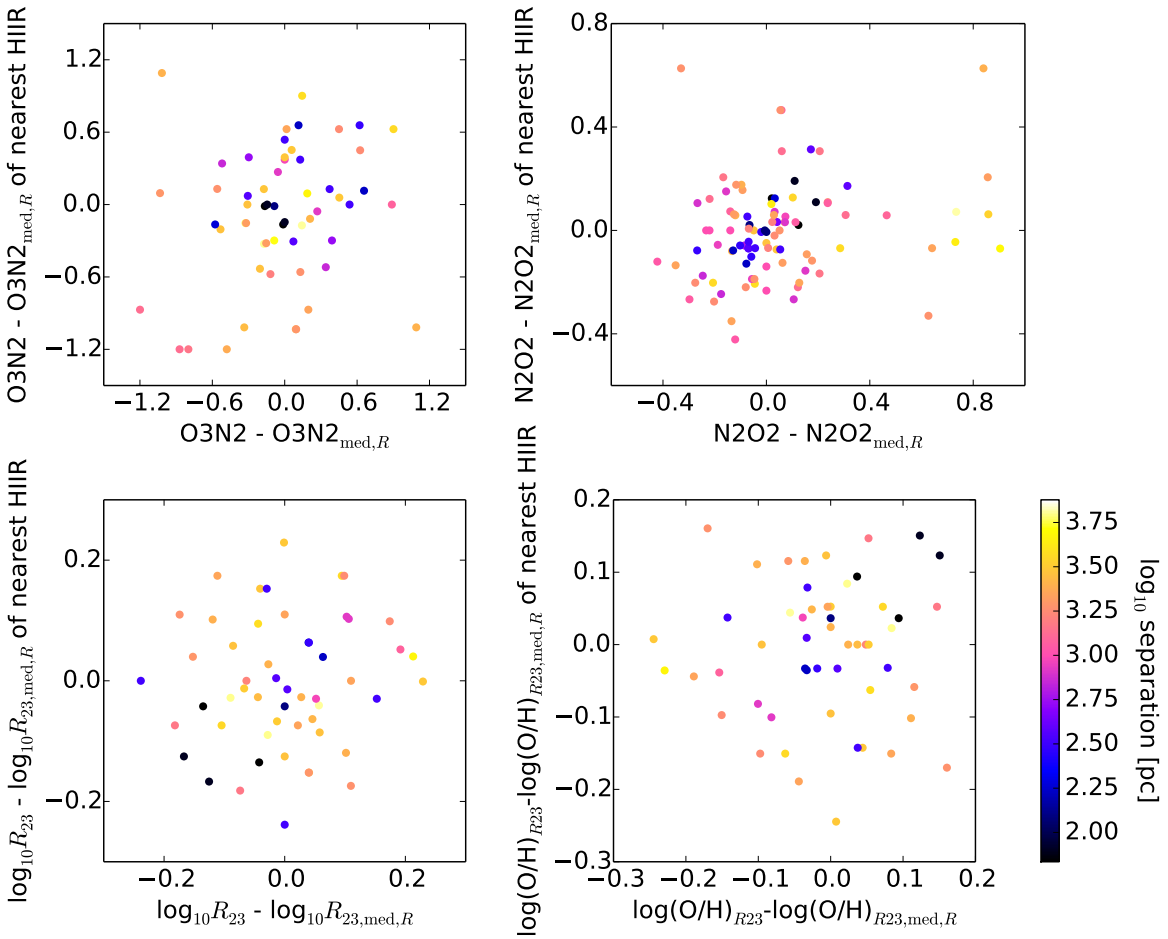

Figure 9. Same as Figure 2, but for O3N2, N2O2, $\log_{10}R_{23}$, and $\log(\mathrm{O/H})_{R23}$ (top left, top right, bottom left, and bottom right panels, respectively).

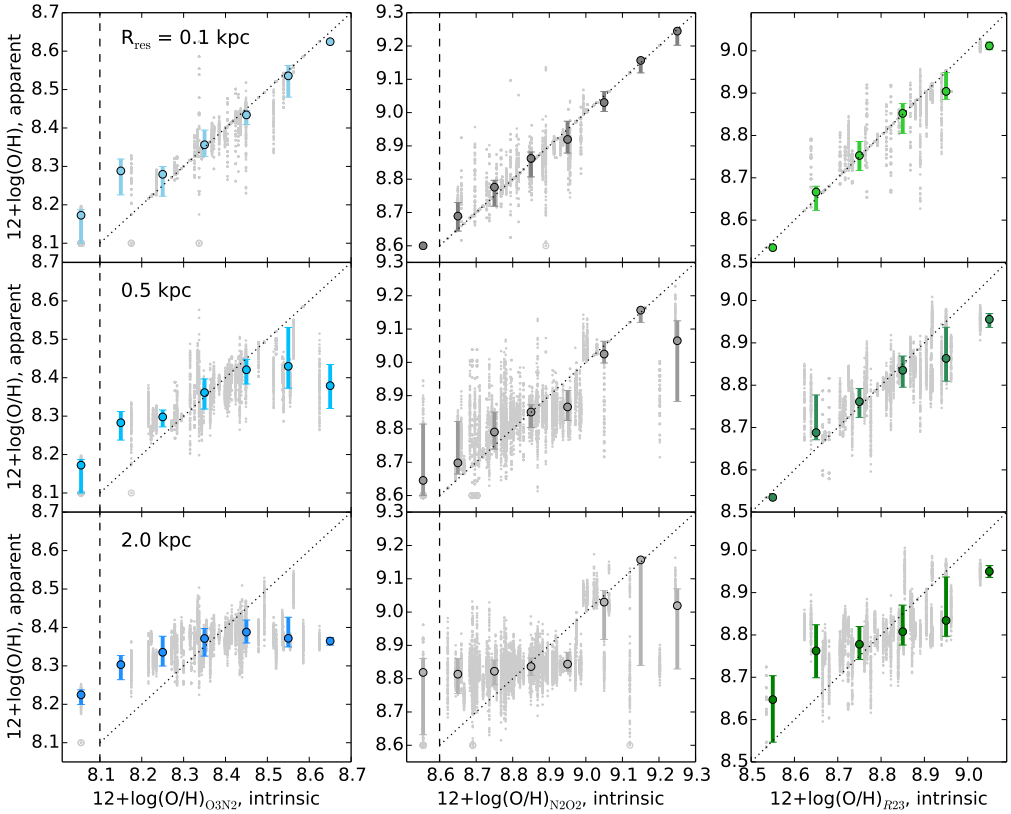

Figure 11. Same as Figure 6, but for the metallicities measured with the O3N2, N2O2, and R_{23} indices (left, middle, and right columns of panels, respectively). Results for $R_{\rm res}$ = 0.1, 0.5, and 2.0 kpc are shown in the top, middle, and bottom panels, respectively.

tween the intrinsic and apparent metallicities are more or less consistent with the N2 index case.

When the N2O2 index is used, the HIIRs with intrinsic 12+log(O/H) > 9.0 show a bimodal distribution of apparent metallicities [12+log(O/H) ∼ 8.8 and 9.0] for $R_{\rm res}$ = 0.5, and 2.0 kpc. This is due to the possible multi-peak metallicity distribution of HIIRs at $R_{\rm deproj}$ > 20 kpc which appears only when the N2O2 index is used (the middle panel Figure 8). The HIIRs with intrinsic $12+\log({\rm O/H})_{\rm N2O2} > 9.0$ mainly reside at $R_{\rm deproj}$ = 0–10 kpc, and > 20 kpc. When $R_{\rm res}$ is not small enough to measure the intrinsic metallicities, the HIIRs at $R_{\rm deproj}$ = 0–10 kpc have apparent $12+\log({\rm O/H})_{\rm N2O2} \sim 9.0$, while those at $R_{\rm deproj}$ > 20 kpc have apparent $12+\log({\rm O/H})_{\rm N2O2} \sim 8.8$, which are the typical metallicities in those $R_{\rm deproj}$ bins.

7 IMPLICATIONS FOR GRB/CC SN SITE STUDIES

Many CC SNe are found in the local Universe ($\lesssim$ 100 Mpc), where typical angular resolution of a ground-based optical observation (∼ 1 arcsec) corresponds to $\lesssim$ 500 pc. The metallicities of CC SN sites in the local Universe are usually investigated with spatial resolution of less than a few hundred pc (e.g., Anderson et al. 2010; Sanders et al. 2012b; Kuncarayakti et al. 2013), and our results suggest that the metallicities measured with such spatial resolution can be used as a proxy to study the immediate environment of transient events, if ISM properties of their host galaxies are similar to those in M31. However, there might be systematic differences between the apparent and intrinsic metallicities when the spatial resolution exceeds a few hundred pc.

When we study the transient events whose rate density is much lower than that of CC SNe (e.g., long GRBs, ∼ several $\times 10^{-7}$ yr^{-1}Mpc^{-3}), chances of detecting an event in the local Universe is small, and we need to rely on samples at larger distances. For now, spatially resolved spectra of long GRB sites are obtained for 5 low-redshift GRBs. In Table 1, we summarise the redshifts and relevant emission line fluxes of the sites of these bursts, together with the spatial resolution of each observation. The fluxes are corrected for the extinction in the Milky Way, but not for the host galaxy. The sites of GRB 060505 and 120422A have two sets of emission line fluxes obtained independently. Although the emission line fluxes of the site of GRB 120422A corrected for the host galaxy extinction are provided in Levesque et al. (2012), we undo this correction for consistency with other data.

In Table 2, we show E_{B-V} in the host galaxy, and the site metallicities measured with the N2, O3N2, N2O2, and R_{23} indices computed from the line fluxes listed in Table 1. The value of E_{B-V} is obtained using Hα/Hβ line ratio assuming the intrinsic value of Hα/Hβ = 2.85 and the Cardelli extinction curve. The metallicity indices are extinction corrected accordingly. When the index values are outside of

Table 1. Emission lines observed at long GRB sites in the literature. The line fluxes are from GRB 980425: Christensen et al. (2008), 020819: Levesque et al. (2010), 060505: Thöne et al. (2008), Thöne et al. (2014), 100316D: Levesque et al. (2011), 120422A: Levesque et al. (2012), and Schulze et al. (2014), in units of 10^{-16} erg s^{-1} cm^{-2}. The flux errors are typically ~ 10 per cent unless otherwise specified.

GRB	redshift	spatial resolution [kpc][a]	[O II] λ3727	Hβ	[O III] λ4959	[O III] λ5007	Hα	[N II]
980425	0.0085	0.27[b]	26.07	7.55	-	18.27	44.94	5.03
020819	0.41	3.0	0.92	-	-	-	4.14	1.51
060505[c]	0.089	1.2	1.12	0.298	0.284	0.72	0.973	0.096
		2.2	2.39±0.13	1.15±0.07	0.76±0.08	1.98±0.06	3.11±0.07	0.24±0.03
100316D	0.059	1.0	-	90±10	-	280±10	200±10	12±10
120422A[d]	0.283	3.0	0.99±0.07	0.16±0.01	< 0.11	0.42±0.03	0.62±0.04	< 0.08
		4.2	0.25±0.01	0.05±0.04	0.05±0.02	0.19±0.02	0.24±0.01	0.06±0.02

[a] Diameter of seeing size unless otherwise specified.
[b] Diameter of the integral field unit resolution element (Christensen et al. 2008).
[c] Two independent sets of emission line fluxes are obtained for the site of GRB 060505 by Thöne et al. (2008, upper row) & Thöne et al. (2014, lower row)
[d] Two independent sets of emission line fluxes are obtained for the site of GRB 120422A by Levesque et al. (2012, upper row) & Schulze et al. (2014, lower row)

the calibrated range, we show the index value instead of the metallicities. It is clear that the different metallicity calibration methods give different metallicities for the same GRB sites, and thus we compare the metallicities of the GRB sites only when they are obtained by the same calibration method.

The explosion site of GRB 980425 is the only one which is spectroscopically observed with a comparable spatial resolution to $R_{\rm res} \sim 0.1\,$kpc owing to its close distance of $z = 0.0085$ (Christensen et al. 2008). With the N2 index, the explosion site metallicity of this burst is $12+\log({\rm O/H})_{\rm N2} = 8.30$ with the calibration by Marino et al. (2013). In the other cases, the spatial resolution is $\gtrsim 1\,$kpc, and our results suggest that there might be systematic differences between the observed and the actual metallicity.

The sites of GRB 020819 and 120422A (Levesque et al. 2010; Schulze et al. 2014) have higher metallicities than other explosion sites when the N2 index is used [$12+\log({\rm O/H})_{\rm N2} \sim 8.5$ which is similar to the typical metallicity of M31 HIIRs], although the independent spectroscopy of the GRB 120422A site by Levesque et al. (2012) indicates a lower metallicity with the same metallicity calibration method but with different slit alignment and seeing size (N2 < -0.89 by Levesque et al. 2012, N2 $= -0.60^{+0.12}_{-0.18}$ by Schulze et al. 2014). The site of GRB 060505 (Thöne et al. 2014) also shows a high metallicity when the R_{23} index is used, although the metallicity of this site is similar to the other sites when measured with other indices. A lower metallicity is independently suggested also at the GRB 060505 site using the emission line fluxes obtained by Thöne et al. (2008). As mentioned in §6, the calibration methods using the R_{23} index provides two possible solutions of metallicities. According to the photoionization model of KK04, N2 $= -1.1$–-1.0 and $O_{32} = 0.9$–1.1 obtained at the GRB 060505 site suggests that the upper branch solution [$12+\log({\rm O/H})_{R23} > 8.4$] is the correct one.

The GRB sites with high metallicities are especially interesting in the context of GRB progenitor studies, casting doubts on the low metallicities of GRB progenitors predicted by some theoretical studies (e.g., Yoon & Langer 2005; Woosley & Heger 2006). However, the high-metallicity GRB sites are currently found only by the spectroscopic observations with spatial resolution of $> 2\,$kpc. In our analysis, these spatial resolution correspond to the cases with $R_{\rm res} \geqslant 1.0\,$kpc, where one cannot distinguish low and high metallicities. Thus the observed high metallicities could be significantly different from the true values in the immediate environment of the GRBs.

We note that the metallicity of the GRB host galaxies are also studied via absorption lines in the GRB afterglow spectra (e.g., Fynbo et al. 2008; Savaglio et al. 2009; Cucchiara et al. 2014), and high metallicities are found in some cases (e.g., Savaglio et al. 2012). However, the absorption line study would give the metallicity averaged over the line-of-sight in the host galaxy, and its relation with the metallicity in the immediate environment of a GRB is not understood well.

8 CONCLUSIONS

In this paper we examine how the small-scale metallicity variation in a galaxy affects the observations of GRB/CC SN sites with limited spatial resolution, using the observational data of M31 HIIRs as a template of metallicity variation in a late-type galaxy. Our results suggest that, when the GRB/CC SN sites are resolved down to $R_{\rm res} \lesssim 500\,$pc scale, the estimated apparent metallicities (or emission-line ratios) do reflect the immediate environment of the transient events, but with significant systematic errors. If $R_{\rm res} \lesssim 100\,$pc, the measured metallicity correlates with the intrinsic one tightly.

The CC SN site studies are often conducted in the local Universe ($< 100\,$Mpc), and we can achieve $R_{\rm res} \lesssim$ a few hundred pc. On the other hand, the detections of transient events with low event rate density (e.g., long GRBs) are

Table 2. Extinctions and metallicities of the long GRB sites computed from the emission-line fluxes listed in Table 1. For the sites of GRB 020819 (Levesque et al. 2010) and GRB 120422A (as observed by Schulze et al. 2014), we only use the N2 index to measure the metallicities due to the non-detection or the large flux errors in Hβ, and the resulting poor constraint on E_{B-V}.

GRB	E_{B-V}	12+log(O/H)$_{\rm N2}$	12+log(O/H)$_{\rm O3N2}$	12+log(O/H)$_{\rm N2O2}$	12+log(O/H)$_{R23}$
980425	0.74±0.13	8.30	8.26	(N2O2 = −1.39)	($\log_{10}R_{23} = 0.99$, $\log_{10}O_{32} = -0.54$)
020819	-	8.54	-	-	-
060505	0.13±0.13	8.28	8.24	(N2O2 = −1.3–−1.1)	8.51
	0.0	8.23	8.24	(N2O2 = −1.0)	8.82
100316D	0.0	8.18	8.17	-	-
120422A	0.31±0.09	< 8.33	< 8.26	(N2O2 < -1.37)	($\log_{10}R_{23} = 1.04$, $\log_{10}O_{32} = -0.53$)
	0.0–1.1	8.47	-	-	-

rare in the local Universe, and we need to rely on a sample at higher redshifts, where $R_{\rm res} \gtrsim$ a few kpc typically. With such low spatial resolution, our results suggest that it is difficult to constrain the site metallicities accurately, and the measured HIIR metallicities will be close to the average metallicity of the host galaxy due to the blending within the spatial resolution.

However, we would like to emphasize that the overall properties of host galaxies are still important clues to the nature of transient progenitors. For example, the transient events that originate from low-metallicity stars would occur preferentially (but not exclusively) in low-metallicity galaxies.

Some of the host galaxies of long GRBs and the explosion sites are found to have high metallicities with limited spatial resolution of $\gtrsim$ a few kpc (e.g., Levesque et al. 2010; Niino et al. 2012; Elliott et al. 2013; Schulze et al. 2014; Hashimoto et al. 2014). However, low-metallicity star formation could still take place in a host galaxy with a high averaged metallicity. In fact, Niino (2011) showed that up to ~ 25 per cent of cosmic low-metallicity star formation in the local Universe takes place in high-metallicity galaxies with 12+log(O/H) > 8.8. This means that *the above observations do not rule out the hypothesis that long GRBs are exclusively born in a low-metallicity environment, as suggested by the stellar evolution models* (e.g., Yoon & Langer 2005; Woosley & Heger 2006).

Our results are based only on the observed statistical properties of the HIIRs in M31, however, HIIRs in other galaxies may have different properties to the M31 HIIRs. Many GRB host galaxies are in fact dwarf irregulars that actively form stars (e.g., Fruchter et al. 2006), and it is likely that they have different ISM properties to that of the spiral galaxies like M31. At the same time, some host galaxies of long GRBs are spiral galaxies, which often have higher masses and metallicities than dwarf irregulars. These spiral galaxies are especially interesting in the context of metallicity dependence of long-GRB occurrence, and they may have similar HIIR properties to M31. Larger spectroscopic samples of HIIRs with very high spatial resolution of a few 10 pc, as recently done by Sánchez et al. (2014), in dwarf irregulars and other types of galaxies are necessary to further discuss the relation between the apparent and intrinsic metallicities in more general population of host galaxies.

With a seeing size of ~ 1 arcsec, which is typical of ground-based optical observations, we can achieve the spatial resolution of $R_{\rm res} < 1$ kpc only at redshifts < 0.1. To investigate the immediate environments of transients at $z \gtrsim 0.1$ with sufficient spatial resolution, we need observations with space telescopes. Observations in different wavelengths other than the optical may also be a solution once good metallicity diagnostics are found, although currently there are no known metallicity diagnostics in the wavelength ranges where we can achieve high spatial resolution from the ground (e.g., in near-infrared with adaptive optics or in radio with interferometers) unless they are significantly redshifted (e.g., Giveon et al. 2002; Nagao et al. 2012).

ACKNOWLEDGMENTS

We would like to thank our referee, Ángel R, López-Sánchez, for his helpful comments. We also thank Antonino Cucchiara, Raffaella Margutti, Maryam Modjaz, Nathan Sanders, and Francesco Taddia for their useful comments. Y.N. is supported by the Research Fellowship for Young Scientists from the Japan Society for the Promotion of Science (JSPS).

REFERENCES

Afflerbach A., Churchwell E., Werner M. W., 1997, ApJ, 478, 190
Anderson J. P., Covarrubias R. A., James P. A., Hamuy M., Habergham S. M., 2010, MNRAS, 407, 2660
Azimlu M., Marciniak R., Barmby P., 2011, AJ, 142, 139 (A11)
Baade W., Arp H., 1964, ApJ, 139, 1027
Balser D. S., Rood R. T., Bania T. M., Anderson L. D., 2011, ApJ, 738, 27
Belfiore F., Maiolino R., Bundy K., Thomas D., Maraston C., Wilkinson D., Sánchez S. F., Bershady M., Blanc G. A., Bothwell M., et al., 2014, ArXiv e-prints
Blanc G. A., Weinzirl T., Song M., Heiderman A., Gebhardt K., Jogee S., Evans II N. J., van den Bosch R. C. E., Luo R., Drory N., Fabricius M., Fisher D., Hao L., Kaplan K., Marinova I., Vutisalchavakul N., Yoachim P., 2013, AJ, 145, 138
Bresolin F., Ryan-Weber E., Kennicutt R. C., Goddard Q., 2009, ApJ, 695, 580

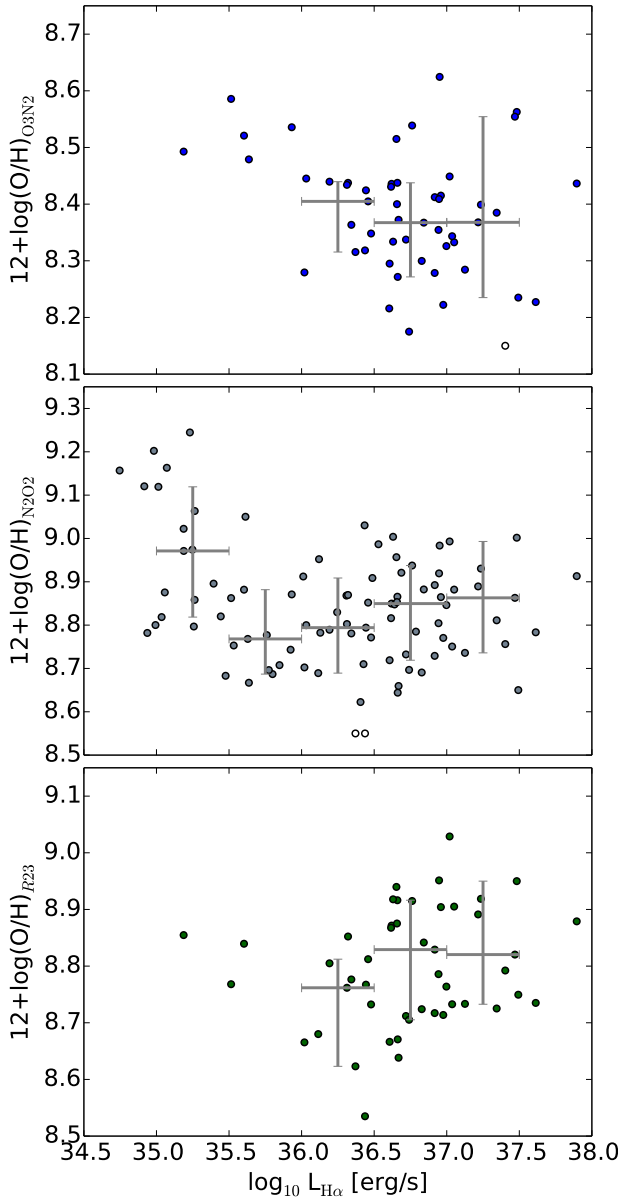

Figure 10. Same as Figure 5, but for the metallicities measured with O3N2, N2O2, and R_{23} indices (top, middle, and bottom panels, respectively).

Cardelli J. A., Clayton G. C., Mathis J. S., 1989, ApJ, 345, 245

Christensen L., Vreeswijk P. M., Sollerman J., Thöne C. C., Le Floc'h E., Wiersema K., 2008, A&A, 490, 45

Cucchiara A., Fumagalli M., Rafelski M., Kocevski D., Prochaska J. X., Cooke R. J., Becker G. D., 2014, ArXiv e-prints

Dufour R. J., Harlow W. V., 1977, ApJ, 216, 706

Elliott J., Krühler T., Greiner J., Savaglio S., Olivares F., Rau E. A., de Ugarte Postigo A., Sánchez-Ramírez R., Wiersema K., Schady P., et al., 2013, A&A, 556, A23

Esteban C., Carigi L., Copetti M. V. F., García-Rojas J., Mesa-Delgado A., Castañeda H. O., Péquignot D., 2013, MNRAS, 433, 382

Fogarty L. M. R., Bland-Hawthorn J., Croom S. M., Green A. W., Bryant J. J., Lawrence J. S., Richards S., Allen J. T., Bauer A. E., Birchall M. N., et al., 2012, ApJ, 761, 169

Freedman W. L., Madore B. F., 1990, ApJ, 365, 186

Fruchter A. S., Levan A. J., Strolger L., Vreeswijk P. M., Thorsett S. E., Bersier D., Burud I., Castro Cerón J. M., Castro-Tirado A. J., Conselice C., Dahlen T., Ferguson H. C., Fynbo J. P. U., et al., 2006, Nature, 441, 463

Fynbo J. P. U., Prochaska J. X., Sommer-Larsen J., Dessauges-Zavadsky M., Møller P., 2008, ApJ, 683, 321

Galbany L., Stanishev V., Mourão A. M., Rodrigues M., Flores H., García-Benito R., Mast D., Mendoza M. A., Sánchez S. F., Badenes C., the CALIFA Collaboration 2014, ArXiv e-prints

Garnett D. R., 1992, AJ, 103, 1330

Giveon U., Sternberg A., Lutz D., Feuchtgruber H., Pauldrach A. W. A., 2002, ApJ, 566, 880

Graham J. F., Fruchter A. S., 2013, ApJ, 774, 119

Hashimoto T., Perley D. A., Ohta K., Aoki K., Tanaka I., Niino Y., Yabe K., Kawai N., 2014, ArXiv e-prints

Kelly P. L., Kirshner R. P., Pahre M., 2008, ApJ, 687, 1201

Kennicutt Jr. R. C., Bresolin F., Garnett D. R., 2003, ApJ, 591, 801

Kewley L. J., Dopita M. A., 2002, ApJS, 142, 35 (KD02)

Kewley L. J., Ellison S. L., 2008, ApJ, 681, 1183

Kobulnicky H. A., Kewley L. J., 2004, ApJ, 617, 240 (KK04)

Kuncarayakti H., Doi M., Aldering G., Arimoto N., Maeda K., Morokuma T., Pereira R., Usuda T., Hashiba Y., 2013, AJ, 146, 30

Lebouteiller V., Bernard-Salas J., Brandl B., Whelan D. G., Wu Y., Charmandaris V., Devost D., Houck J. R., 2008, ApJ, 680, 398

Leloudas G., Gallazzi A., Sollerman J., Stritzinger M. D., Fynbo J. P. U., Hjorth J., Malesani D., Michałowski M. J., Milvang-Jensen B., Smith M., 2011, A&A, 530, A95

Leloudas G., Sollerman J., Levan A. J., Fynbo J. P. U., Malesani D., Maund J. R., 2010, A&A, 518, A29

Levesque E. M., Berger E., Soderberg A. M., Chornock R., 2011, ApJ, 739, 23

Levesque E. M., Chornock R., Soderberg A. M., Berger E., Lunnan R., 2012, ApJ, 758, 92

Levesque E. M., Kewley L. J., Graham J. F., Fruchter A. S., 2010, ApJL, 712, L26

López-Sánchez Á. R., Dopita M. A., Kewley L. J., Zahid H. J., Nicholls D. C., Scharwächter J., 2012, MNRAS, 426, 2630

López-Sánchez Á. R., Esteban C., 2010, A&A, 517, A85

López-Sánchez Á. R., Mesa-Delgado A., López-Martín L., Esteban C., 2011, MNRAS, 411, 2076

Luck R. E., Gieren W. P., Andrievsky S. M., Kovtyukh V. V., Fouqué P., Pont F., Kienzle F., 2003, A&A, 401, 939

Lunnan R., Chornock R., Berger E., Laskar T., Fong W., Rest A., Sanders N. E., Challis P. M., Drout M. R., Foley R. J., Huber M. E., et al., 2014, ApJ, 787, 138

Maiolino R., Nagao T., Grazian A., Cocchia F., Marconi A., Mannucci F., Cimatti A., Pipino A., Ballero S., Calura F., et al., 2008, A&A, 488, 463

Marino R. A., Rosales-Ortega F. F., Sánchez S. F., Gil

de Paz A., Vílchez J., Miralles-Caballero D., Kehrig C., Pérez-Montero E., Stanishev V., Iglesias-Páramo J., et al., 2013, A&A, 559, A114
Mármol-Queraltó E., Sánchez S. F., Marino R. A., Mast D., Viironen K., Gil de Paz A., Iglesias-Páramo J., Rosales-Ortega F. F., Vilchez J. M., 2011, A&A, 534, A8
Massey P., McNeill R. T., Olsen K. A. G., Hodge P. W., Blaha C., Jacoby G. H., Smith R. C., Strong S. B., 2007, AJ, 134, 2474
Massey P., Olsen K. A. G., Hodge P. W., Strong S. B., Jacoby G. H., Schlingman W., Smith R. C., 2006, AJ, 131, 2478
Matonick D. M., Fesen R. A., 1997, ApJS, 112, 49
McGaugh S. S., 1991, ApJ, 380, 140
Mesa-Delgado A., Esteban C., 2010, MNRAS, 405, 2651
Mesa-Delgado A., Esteban C., García-Rojas J., 2008, ApJ, 675, 389
Modjaz M., Kewley L., Bloom J. S., Filippenko A. V., Perley D., Silverman J. M., 2011, ApJL, 731, L4
Modjaz M., Kewley L., Kirshner R. P., Stanek K. Z., Challis P., Garnavich P. M., Greene J. E., Kelly P. L., Prieto J. L., 2008, AJ, 135, 1136
Nagao T., Maiolino R., De Breuck C., Caselli P., Hatsukade B., Saigo K., 2012, A&A, 542, L34
Nagao T., Maiolino R., Marconi A., 2006, A&A, 459, 85
Niino Y., 2011, MNRAS, 417, 567
Niino Y., Hashimoto T., Aoki K., Hattori T., Yabe K., Nomoto K., 2012, PASJ, 64, 115
Pagel B. E. J., Edmunds M. G., Fosbury R. A. E., Webster B. L., 1978, MNRAS, 184, 569
Pilyugin L. S., 2000, A&A, 362, 325
Richards S. N., Schaefer A. L., López-Sánchez Á. R., Croom S. M., Bryant J. J., Sweet S. M., Konstantopoulos I. S., Allen J. T., Bland-Hawthorn J., Bloom J. V., Brough S., et al., 2014, MNRAS, 445, 1104
Rosales-Ortega F. F., Kennicutt R. C., Sánchez S. F., Díaz A. I., Pasquali A., Johnson B. D., Hao C. N., 2010, MNRAS, 405, 735
Rosolowsky E., Simon J. D., 2008, ApJ, 675, 1213
Sánchez S. F., Galbany L., Pérez E., Sánchez-Blázquez P., Falcón-Barroso J., Rosales-Ortega F. F., Sánchez-Menguiano L., Marino R., Kuncarayakti H., Anderson J. P., Kruehler T., et al., 2014, ArXiv e-prints
Sánchez S. F., Kennicutt R. C., Gil de Paz A., van de Ven G., Vílchez J. M., Wisotzki L., Walcher C. J., Mast D., Aguerri J. A. L., Albiol-Pérez S., Alonso-Herrero A., et al., 2012, A&A, 538, A8
Sanders N. E., Caldwell N., McDowell J., Harding P., 2012c, ApJ, 758, 133 (S12)
Sanders N. E., Levesque E. M., Soderberg A. M., 2013, ApJ, 775, 125
Sanders N. E., Soderberg A. M., Levesque E. M., Foley R. J., Chornock R., Milisavljevic D., Margutti R., Berger E., Drout M. R., Czekala I., Dittmann J. A., 2012b, ApJ, 758, 132
Sanders N. E., Soderberg A. M., Valenti S., Foley R. J., Chornock R., Chomiuk L., Berger E., Smartt S., Hurley K., Barthelmy S. D., et al., 2012a, ApJ, 756, 184
Savaglio S., Glazebrook K., Le Borgne D., 2009, ApJ, 691, 182
Savaglio S., Rau A., Greiner J., Krühler T., McBreen S., Hartmann D. H., Updike A. C., Filgas R., Klose S., Afonso P., Clemens C., Küpcü Yoldaş A., Olivares E. F., Sudilovsky V., Szokoly G., 2012, MNRAS, 420, 627
Schulze S., Malesani D., Cucchiara A., Tanvir N. R., Krühler T., de Ugarte Postigo A., Leloudas G., Lyman J., Bersier D., Wiersema K., Perley D. A., et al., 2014, A&A, 566, A102
Shields G. A., Searle L., 1978, ApJ, 222, 821
Simien F., Pellet A., Monnet G., Athanassoula E., Maucherat A., Courtes G., 1978, A&A, 67, 73
Stanek K. Z., Gnedin O. Y., Beacom J. F., Gould A. P., Johnson J. A., Kollmeier J. A., Modjaz M., Pinsonneault M. H., Pogge R., Weinberg D. H., 2006, Acta Astronomica, 56, 333
Taddia F., Sollerman J., Razza A., Gafton E., Pastorello A., Fransson C., Stritzinger M. D., Leloudas G., Ergon M., 2013, A&A, 558, A143
Thöne C. C., Christensen L., Prochaska J. X., Bloom J. S., Gorosabel J., Fynbo J. P. U., Jakobsson P., Fruchter A. S., 2014, MNRAS, 441, 2034
Thöne C. C., Fynbo J. P. U., Östlin G., Milvang-Jensen B., Wiersema K., Malesani D., Della Monica Ferreira D., Gorosabel J., Kann D. A., Watson D., Michałowski M. J., Fruchter A. S., Levan A. J., Hjorth J., Sollerman J., 2008, ApJ, 676, 1151
Vermeij R., Damour F., van der Hulst J. M., Baluteau J.-. P., 2002, A&A, 390, 649
Woosley S. E., Heger A., 2006, ApJ, 637, 914
Yoon S., Langer N., 2005, A&A, 443, 643
Yoon S., Langer N., Norman C., 2006, A&A, 460, 199
Zaritsky D., Kennicutt Jr. R. C., Huchra J. P., 1994, ApJ, 420, 87

This paper has been typeset from a TEX/ LATEX file prepared by the author.